

GAN-based metal artifacts region inpainting in brain MRI imaging with reflective registration

Kai Xie^{1,2} | Liugang Gao^{1,2} | Heng Zhang^{3,4} | Sai Zhang^{3,4} | Qianyi Xi^{3,4} | Fan Zhang^{3,4} | Jiawei Sun^{1,2} | Tao Lin^{1,2} | Jianfeng Sui^{1,2} | Xinye Ni^{1,2,3,4}

¹Radiotherapy Department, Second People's Hospital of Changzhou, Nanjing Medical University, Changzhou, China

²Jiangsu Province Engineering Research Center of Medical Physics, Changzhou, China

³Center for Medical Physics, Nanjing Medical University, Changzhou, China

⁴Changzhou Key Laboratory of Medical Physics, Changzhou, China

Correspondence

Xinye Ni, Radiotherapy Department, Second People's Hospital of Changzhou, Nanjing Medical University, Changzhou, China.
Email: nxy@njmu.edu.cn

Funding information

National Natural Science Foundation of China, Grant/Award Number: 62371243; Changzhou Sci&Tech Program, Grant/Award Numbers: CJ20200099, CJ20210128, CJ20220136, CE20235063; Science and Technology Programs for Young Talents of Changzhou Health Commission, Grant/Award Number: QN201932; Young Talent Development Plan of Changzhou Health Commission, Grant/Award Numbers: CZQM2020075, CZQM2020067; General Program of Jiangsu Provincial Health Commission, Grant/Award Number: M2020006; Jiangsu Provincial Key Research and Development Program Social Development, Grant/Award Number: BE2022720; Jiangsu Provincial Medical Key Discipline Cultivation Unit of Oncology Therapeutics, Grant/Award Number: JSWD202237

Abstract

Background and objective: Metallic magnetic resonance imaging (MRI) implants can introduce magnetic field distortions, resulting in image distortion, such as bulk shifts and signal-loss artifacts. Metal Artifacts Region Inpainting Network (MARINet), using the symmetry of brain MRI images, has been developed to generate normal MRI images in the image domain and improve image quality.

Methods: T1-weighted MRI images containing or located near the teeth of 100 patients were collected. A total of 9000 slices were obtained after data augmentation. Then, MARINet based on U-Net with a dual-path encoder was employed to inpaint the artifacts in MRI images. The input of MARINet contains the original image and the flipped registered image, with partial convolution used concurrently. Subsequently, we compared PConv with partial convolution, and GConv with gated convolution, SDEdit using a diffusion model for inpainting the artifact region of MRI images. The mean absolute error (MAE) and peak signal-to-noise ratio (PSNR) for the mask were used to compare the results of these methods. In addition, the artifact masks of clinical MRI images were inpainted by physicians.

Results: MARINet could directly and effectively inpaint the incomplete MRI images generated by masks in the image domain. For the test results of PConv, GConv, SDEdit, and MARINet, the masked MAEs were 0.1938, 0.1904, 0.1876, and 0.1834, respectively, and the masked PSNRs were 17.39, 17.40, 17.49, and 17.60 dB, respectively. The visualization results also suggest that the network can recover the tissue texture, alveolar shape, and tooth contour. Additionally, for clinical artifact MRI images, MARINet completed the artifact region inpainting task more effectively when compared with other models.

Conclusions: By leveraging the quasi-symmetry of brain MRI images, MARINet can directly and effectively inpaint the metal artifacts in MRI images in the image domain, restoring the tooth contour and detail, thereby enhancing the image quality.

KEY WORDS

generative adversarial network, image inpainting, metal artifact, MRI, quasi-symmetry

Kai Xie and Liugang Gao contributed equally.

This is an open access article under the terms of the Creative Commons Attribution-NonCommercial License, which permits use, distribution and reproduction in any medium, provided the original work is properly cited and is not used for commercial purposes.

© 2023 The Authors. *Medical Physics* published by Wiley Periodicals LLC on behalf of American Association of Physicists in Medicine.

1 | INTRODUCTION

Magnetic resonance imaging (MRI) has the advantages of good soft tissue resolution, multi-azimuth, multi-parameter imaging, and no ionizing radiation. It has become an essential tool in preoperative diagnosis, positioning, guiding the design of the surgical plan, and postoperative review in head and neck surgery and oral and maxillofacial surgery. Particularly in the oral area, metal implants such as implants, dental crowns, and dental fillings made of precious metal and non-precious metal alloy materials are commonly found in the maxillofacial region. Some metal implants cannot be easily removed.¹ Unfortunately, these metal implants generate magnetic field distortions, resulting in image distortions and producing artifacts in the image. Such interference with displaying normal anatomical structures and diseased tissues makes it challenging to accurately segment the tooth structure, thus affecting clinical diagnosis and analysis.²

The brain MRI atlas is a critical tool in brain imaging research, offering labels for segmentation classification and establishing standardized image data. Brain MRI data containing artifacts may present some new challenges in atlas construction: (1) the artifacts can deform the neighboring tissues and generate a signal void, which makes it challenging to seek alignment with registration; (2) as the artifact region lacks a matching structure in the healthy brain, it becomes unreliable to map the artifact image of a new patient to the previously established atlas space.³ In addition, in PET/MRI, accurate attenuation correction (AC) is a prerequisite for quantitative PET/MRI imaging. A common method is by segmenting MRI into multiple tissue classes. However, the signal void formed by metal artifacts will seriously interfere with tissue segmentation in MRI, which severely underestimates the attenuation and activity concentration observed in PET/MR images.⁴ MRI and CT are often required for registration in radiotherapy, and metal artifacts in MRI will also affect the registration results.⁵ The generation of pseudo-CT from MRI for adaptive radiotherapy has also become a hot spot in clinical research.^{6,7} The metal artifacts in MRI will seriously affect the image quality and accuracy of the generated CT. Consequently, reducing and avoiding the effects of metal artifacts is a high-priority problem.

Traditional metal artifact reduction (MAR) methods include (1) modifying spin echo sequence parameters such as echo time (TE), bandwidth, and slice thickness; (2) using gradient echo sequences with a very short TE; and (3) optimizing metal artifact suppression sequences by adjusting the specific intensity and size of susceptibility artifact.¹ However, applying these methods encounters challenges such as decreasing signal-to-noise ratio (SNR), increasing scanning time, and experiencing residual artifacts after metal artifact correction.^{8,9}

Deep learning has been rapidly applied to medical images and has achieved remarkable results in image classification, segmentation, noise reduction, and generation. In recent years, some researchers have also applied deep learning methods to the MAR of MRI.¹⁰ Kwon et al.¹¹ used U-Net and bipolar readout gradients to reduce metal artifacts and improve the blurring and distortion caused by off-resonance frequencies. Inspired by the former, Kim et al.¹² adopted the attention mechanism and achieved better results. However, it may be challenging to obtain bipolar readout gradient and mechanical parameters for some departments. Liao et al.¹³ proposed an Artifact Disentanglement Network (ADN) for unsupervised MAR. By encoding the artifact and content parts of the image into artifact space and content space, respectively, they are separated to achieve the purpose of CT artifact correction. Multi-modal ADN proposed by Ranzini et al.¹⁴ uses paired MRI and CT images, which can effectively remove the metal artifacts and improve the accuracy of image segmentation. However, it isn't easy to obtain paired images in practical clinical applications. Moreover, the acquired MRI images are challenging to post-process using these methods.

MRI artifact correction presents a significant challenge due to the artifact shape and lack of real label data. In some instances, even though the normal image derived from the artifact image cannot recover the metal information, it still has practical applications. It can be used in the conventional atlas construction process,³ aiding in the recovery of information around the metal, improving registration accuracy, and enhancing the attenuation correction (AC) of PET/MRI. These applications are not only technically innovative but also bear clinical significance. In pursuit of similar studies, Xing et al.³ proposed a deep learning-based image inpainting method to replace tumor regions with normal tissue intensities using only a patient population. At the same time, Liu et al.¹⁵ presented an inpainting network that replaces pathological tumor regions with normal brain appearances, targeting patient-to-normal deformable registration.

In our previous work,¹⁶ we adopted the image inpainting method and treated the artifact area as a hole to recover the missing information caused by metal implants in the image. The brain MRI containing the artifacts is reconstructed into a normal image, which is helpful for subsequent possible image post-processing.³ Meanwhile, in image inpainting studies by deep learning, Pathak et al.¹⁷ proposed the context encoder (CE), which applies generative adversarial network (GAN) into the field of image inpainting for the first time. Iizuka et al.¹⁸ proposed global and local consistency in the foundation of CE. Liu et al.¹⁹ proposed a partial convolution (PC) algorithm in which the mask of each layer is updated to ensure that the convolution is renormalized to be conditioned on only valid pixels. Yu et al.²⁰

proposed a gated convolution (GC) method to focus the convolution operation on effective pixel values by automatically updating the mask. Armanious et al. proposed that ip-MedGAN²¹ and ipA-MedGAN²² could inpaint MRI images with rectangular and arbitrary masks, but they were not used in MRI artifact inpainting.

These inpainting methods were designed to recover the missing areas of the general image and have achieved relatively ideal results.²³ However, when they are used to inpaint metal artifacts of MRI, the inpainting effect is not as satisfactory. The reason behind this is that the MRI image is rich in detail, and these inpainting methods can only recover the artifact area from the information around the artifact area.¹⁶ Unsatisfactory results lead to a fundamental limitation in their application for MRI artifact inpainting. Normal brain MRI images display excellent symmetry in the midsagittal plane, and metal artifacts destroy this quasi-symmetry of MRI. Similarly, doctors often identify brain lesions by relying on the quasi-symmetry of the brain.²⁴ Moreover, symmetry has been recognized as one of the key features of tumor segmentation and has been known to improve segmentation performance.^{25,26} In light of this, although brain MRI images are not perfectly symmetrical, it is feasible to assume that the available information from the other half can be used to simulate the missing information in the artifact region compared with blind guessing.³

In this study, to better recover the information loss caused by denture metal, we introduced symmetry into image inpainting and proposed a dual-path input deep learning framework Metal Artifacts Region Inpainting Network (MARINet) based on U-Net,²⁷ to automatically inpaint the artifact regions in MRI. In addition to the anatomical verification between the inpainted and real images in the test set, we also analyzed the clinical MRI image artifact's inpainting effect to illustrate further the possibility of brain MRI artifact area inpainting using symmetry.

The main contributions of this study are as follows: (1) The original MRI and its reflective registered MRI image were used as the input of the two paths of the MARINet network. (2) We designed a network with a two-path encoder to maximize the use of information around the missing area and its symmetric area. (3) We performed quantitative comparisons and ablation experiments. The network achieved the best results. The mean absolute error (MAE), peak signal-to-noise ratio (PSNR), and structural similarity (SSIM) in the mask were 0.1834, 17.62 dB, and 75.03%, respectively.

2 | METHODS

The whole process of this study, including image preprocessing, network training, and test phases, is shown in Figure 1. T1-weighted MRI images were preprocessed by reflective registration to achieve the average MRI

images. These preprocessed images were introduced into the two encoders of MARINet, and the decoder then acquired the inpainted images.

2.1 | Data acquisition

One hundred patients without dentures who underwent head MRI scans from 2017 to 2021 were selected. This group included 61 males and 39 females, with an average age of 57 ± 9 years and a median age of 58. The study received approval from the ethics association of the Second People's Hospital of Changzhou (2017-002-01). Images were acquired on a Philips Achieva scanner (Philips Healthcare, The Netherlands) using a T1-weighted high-resolution isotropic volume examination sequence. The scanning parameters were as follows: a magnetic field strength of 1.5 T, repetition time of 4.97 ms, TE of 2.46 ms, flip angle of 100°, matrix size of 512×512 , and voxel spacing of $0.49 \times 0.49 \times 2$ mm³. A total of 3000 layers containing or near teeth were collected. Layers from 78, 12, and 12 patients were used for training, verification, and testing, respectively. Data augmentation, such as horizontal and vertical flips, yielded 9000 data layers. MRI images of 20 patients with dentures containing cobalt-chromium alloy were also collected to evaluate the inpaint effect. The pixel value was square-rooted for training and display after normalizing the pixel value since the pixel value concentrated in the range of [0,0.5].

2.2 | Image preprocessing

Most methods in previous literature about symmetry utilize symmetric patches^{24,28} or image flips,²⁵ without accounting for the self-asymmetry and rotation variance of brain images. Inspired by Raina et al.,²⁹ we incorporated brain symmetry information into the MARINet model by introducing additional flip and deformation registration operations to address this. Image inpainting differed from image synthesis in that it involved masking information. During training, multiple masks were applied to the same image to generate corrupted images. However, calculating the reflective registration for each corrupted image was time-consuming, leading to an unacceptably long training period. Therefore, our reflective registration calculation for the training data employed an approximation method, as shown in Figure 1: (1) The left-right flip MRI_f was generated for each original image MRI_{gt}. (2) MRI_{gt} was used as a fixed image, and MRI_f was a moving image. Simpleltk³⁰ was employed for deformation registration using mutual information yielding the registered flipped image referred to as MRI_{fr}. (3) The corrupted images MRI_{gt_m} and MRI_{fr_m} were produced by applying the mask and the left-right flip mask to MRI_{gt} and MRI_{fr}, respectively.

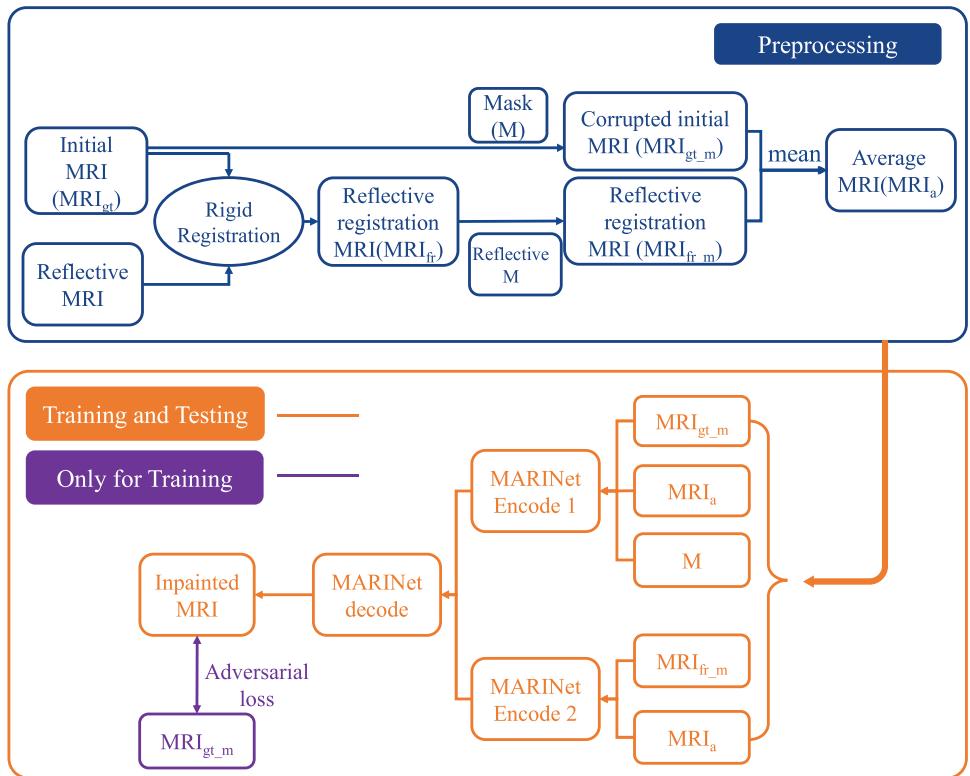


FIGURE 1 Workflow of metal artifacts region inpainting in brain MRI imaging with reflective registration.



FIGURE 2 Description of image reflective registration processing. Left to right are the original image MRI_{gt} , reflective registration image MRI_{fr} , corrupted image $\text{MRI}_{\text{gt_m}}$, reflective registration image $\text{MRI}_{\text{fr_m}}$, and average image MRI_a .

The underlying concept of this approximation method was that the mask was relatively small compared to the whole image, and the deformation field between MRI_{gt} and MRI_{fr} was similar to that between $\text{MRI}_{\text{gt_m}}$ and $\text{MRI}_{\text{fr_m}}$. Further, borrowing from the concept of the average face,³¹ we weighted $\text{MRI}_{\text{gt_m}}$ and $\text{MRI}_{\text{fr_m}}$ to obtain the average image MRI_a , which was also incorporated into the input information. Although MRI_a was derived from MRI_{gt} and MRI_{fr} , it merged information from both, offering helpful reference information for inpainting. Reflective registration was performed on the corrupted image for the test and real clinical artifact data.

Figure 2 illustrates image reflective registration processing, where mask generation was described as follows: 1–3 circles were created by setting random val-

ues to enhance robustness during training. The circle's centers were placed near the tooth with a 25–50 pixels radius to approximate the clinical artifact's shape. For clinical MRI images, the mask corresponding to the artifact area was delineated by a senior physician. The various mask shapes are presented in the Results section.

2.3 | Model architecture

Ordinary convolution was widely employed in tasks such as image classification and synthesis, where all pixels of the input image served to extract local features. However, image inpainting introduced a different scenario, as the

input image contained both effective pixel regions outside the mask and invalid pixels inside the mask. Invalid values within the mask propagated to the decoder stage via vanilla convolution, which might have resulted in unsatisfactory restoration effects, such as color inconsistency and blurred boundaries. To tackle this issue, we utilized PCs in the network and automatically updated the mask through data learning, focusing the operation on the valid pixel value.¹⁹ The implementation method was as follows:

Let W present the convolution filter weights, b the bias, X the feature values for the current convolution window, and M the binary mask. The PC at each location was expressed as:

$$x' = \begin{cases} W^T (X \odot M) \frac{1}{\text{sum}(M)} + b, & \text{if sum}(M) > 0 \\ 0, & \text{otherwise} \end{cases} \quad (1)$$

where \odot denotes element-wise multiplication. As was evident, the output value only depended on the valid pixel value.

Following the PC operation, the mask was set entirely to 1 for any location with at least one valid input value. It was expressed as:

$$m' = \begin{cases} 1, & \text{if sum}(M) > 0 \\ 0, & \text{otherwise} \end{cases} \quad (2)$$

When enough partial convolutional layers were used, any mask would eventually be all 1.

Given a corrupted MRI image, our goal was to synthesize a complete MRI image closely resembling the true appearance. A primary limitation of the above approach was that the missing area inpainting was achieved solely by processing the content of a small neighborhood, which diverged from the manual inpainting process.²⁴ Considering the strong quasi-symmetry of normal brain MRI and that metal dental implants were typically unilateral, the information from the normal symmetry on the other side could be used as a reference during artifact inpainting. Leveraging this understanding, we used reflective registration images as the input to guide image inpainting.

To effectively infer features from both the original image and the reflective registration image, we drew inspiration from Cao et al.³² and employed a dual-path encoder in our U-Net-based MARINet to recover artifact region information, as illustrated in Figure 1. U-Net was initially intended for medical image segmentation but has proven effective in many other image-processing tasks. The generator G in MARINet was an encoding and decoding network which encompassed the original image encoder f_{ori} , the reflective registration image encoder f_{refreg} , the image decoder f_{dec} , and the image discriminator D , as detailed in Figure 3.

The input of f_{ori} included MRI_{gt_m} , MRI_a , and mask M , facilitating better referencing of information around the

missing and symmetric regions. As the input contained M , PC was employed instead of vanilla convolution to concentrate the convolution operation on the effective pixels. As checkerboard artifacts were generated when max-pooling reduced the input size, f_{ori} used eight convolutions with a kernel size of 3×3 and a stride size of 2 to reduce the input size from 512×512 to 2×2 . The number of channels of the convolution kernels was 64, 128, 256, 512, 512, 512, and 512. All convolutional layers used the same padding. The Leaky ReLU function, a variant of the ReLU activation function, provided a slight slope for negative inputs. Batch normalization was an effective method to prevent gradient vanishing and accelerate convergence. Consequently, we added batch normalization and Leaky ReLU (leakiness was 0.2) to each PC layer.

f_{refreg} learned features from the reflective registration image with the input comprising MRI_{fr_m} and MRI_a . For reasons outlined in Section 2.2, the reflective mask was not added to the input, and vanilla convolution was still used. f_{refreg} shared the same structure as f_{ori} , except that PC was replaced with ordinary convolution.

f_{dec} combined the features extracted from f_{ori} and f_{refreg} to reconstruct the missing part. During the upsampling process, the feature map was produced by partial deconvolution with a kernel size of 3×3 and a stride size of 2, and it was concatenated with the feature map of the same size from f_{ori} and f_{refreg} . The inpainted image was obtained using the tanh function in the final output.

PatchGAN³³ served as the discriminator D in MARINet, as depicted in Figure 4. Following two convolutions with a kernel size of 4×4 and a stride size of 2, the input size reduced from 512×512 to 64×64 , and the number of convolution kernel channels was 64 and 128, respectively. The final output feature map was acquired through three convolutions with a kernel size of 4×4 and a stride size of 1, and the number of convolution kernel channels was 256, 512, and 1, respectively. Except for the sigmoid function added after the final convolution operation, batch normalization and Leaky ReLU (leakiness was 0.2) were incorporated after other convolution operations. The output probability used 1 to represent real images and 0 to denote inpainted images.

The loss function for MARINet included adversarial loss, L1 loss function, gradient loss, and symmetric loss function. The adversarial loss function employed the loss function from the Least Squares Generative Adversarial Network.³⁴ For the generator and discriminator, these losses were as follows:

$$L_{G_adv} = E_X [(D(G(X)) - 1)^2] \quad (3)$$

and

$$L_{D_adv} = E_Y [(D(Y) - 1)^2] + E_X [(D(G(X))^2)] \quad (4)$$

where X is the incomplete image, and Y is the real image.

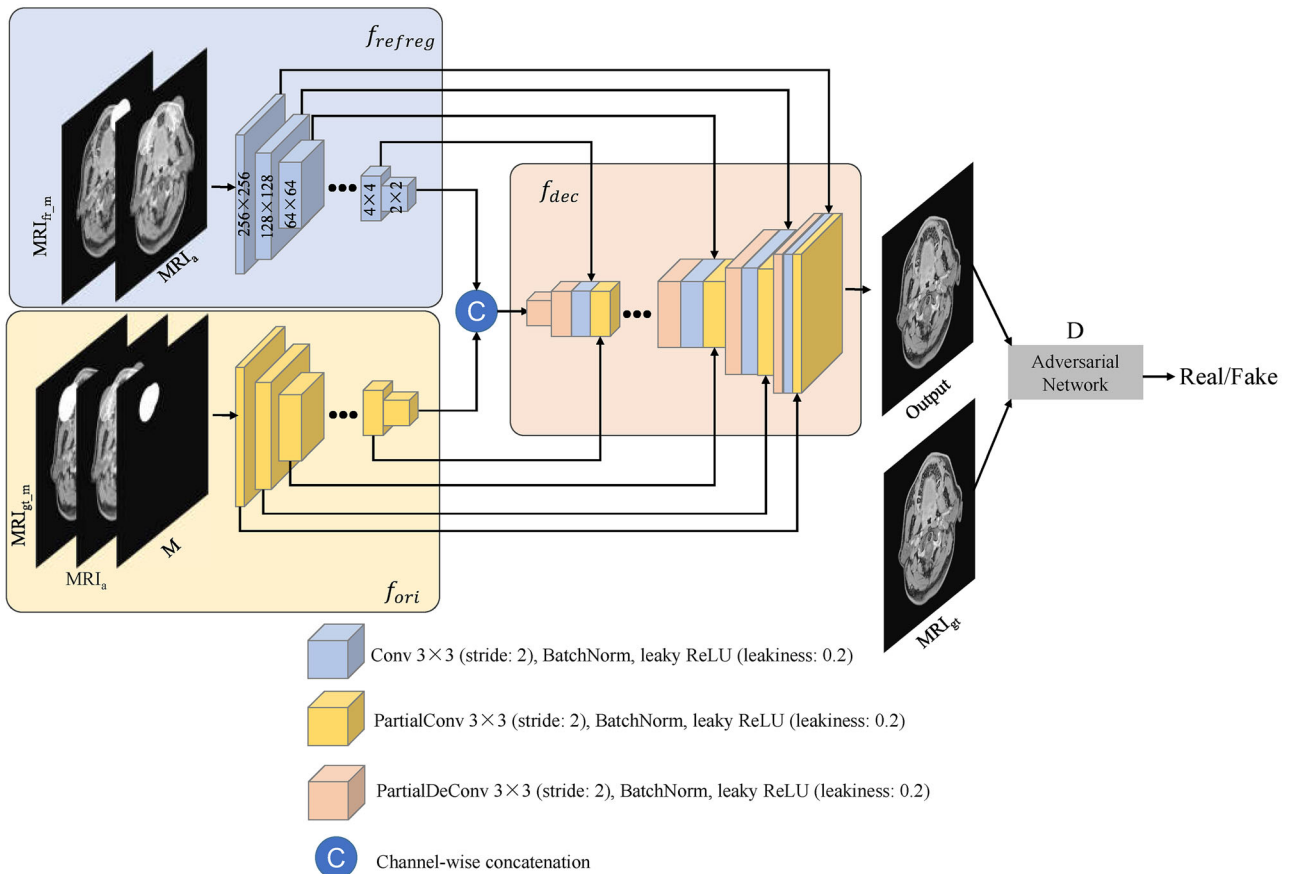


FIGURE 3 Structure diagram of the metal artifact area of the MRI image inpainted by MARINet. MRI_{gt} : the original image, MRI_{fr} : the reflective registration image, $\text{MRI}_{\text{gt_m}}$: corrupted image, $\text{MRI}_{\text{fr_m}}$: reflective registration image, and MRI_a : average image.

The L1 loss was defined as follows:

$$L_1 = E_{X,Y} [|Y - G(X)|] \quad (5)$$

The gradient loss term further ensured the gradient similarity between the inpainted and real images, rendering the texture information as accurate as possible and addressing the image blur problem induced by the L1 loss term.³⁵ The gradient loss was defined as follows:

$$L_{GL} = E_{X,Y} \left[(\nabla G(X)_x - \nabla Y_x)^2 + (\nabla G(X)_y - \nabla Y_y)^2 \right] \quad (6)$$

Given the significant symmetry between the left and right sides of the brain MRI, but not complete symmetry, that is, “quasi-symmetry”, using this anatomical symmetry constraint in the inpainting image could reduce the ill-posed repair task and enhance the repair effect.¹⁵ The symmetric loss function was defined as follows:

$$L_{sym} = E_{X,Y_{fr}} [|Y_{fr} - G(X)|] \quad (7)$$

where Y_{fr} is the reflective registration image from Y .

The final loss function of the generator was:

$$L_G = L_{G_adv} + \lambda_1 L_1 + \lambda_2 L_{GL} + \lambda_3 L_{sym} \quad (8)$$

where λ_1 , λ_2 , and λ_3 were the weight parameters.

Additionally, PConv,¹⁹ GConv,²⁰ and Stochastic Differential Editing (SDEdit)³⁶ were trained and utilized for artifact inpainting, in which the inputs were $\text{MR}_{\text{gt_m}}$, MR_a , and M , and the inpainting results of different models were compared. Denoising Diffusion Probabilistic Models (DDPM)³⁷ is an emerging alternative method for image generation. SDEdit was based on a diffusion model generative prior and synthesized realistic images by iterative denoising through a stochastic differential equation (SDE).³⁸ More details can be found in the original article for a comprehensive understanding of these methods.

The networks were trained on two NVIDIA GeForce RTX 3090 GPU cards with 48 GB memory. GatedConv was built using TensorFlow, while PConv, SDEdit, and MARINet were built by PyTorch. The training epoch for all methods was 200, and the batch sizes for PConv, GatedConv, SDEdit, and MARINet were 32, 16, 8, and 16, respectively. The Adam optimizer was used with a

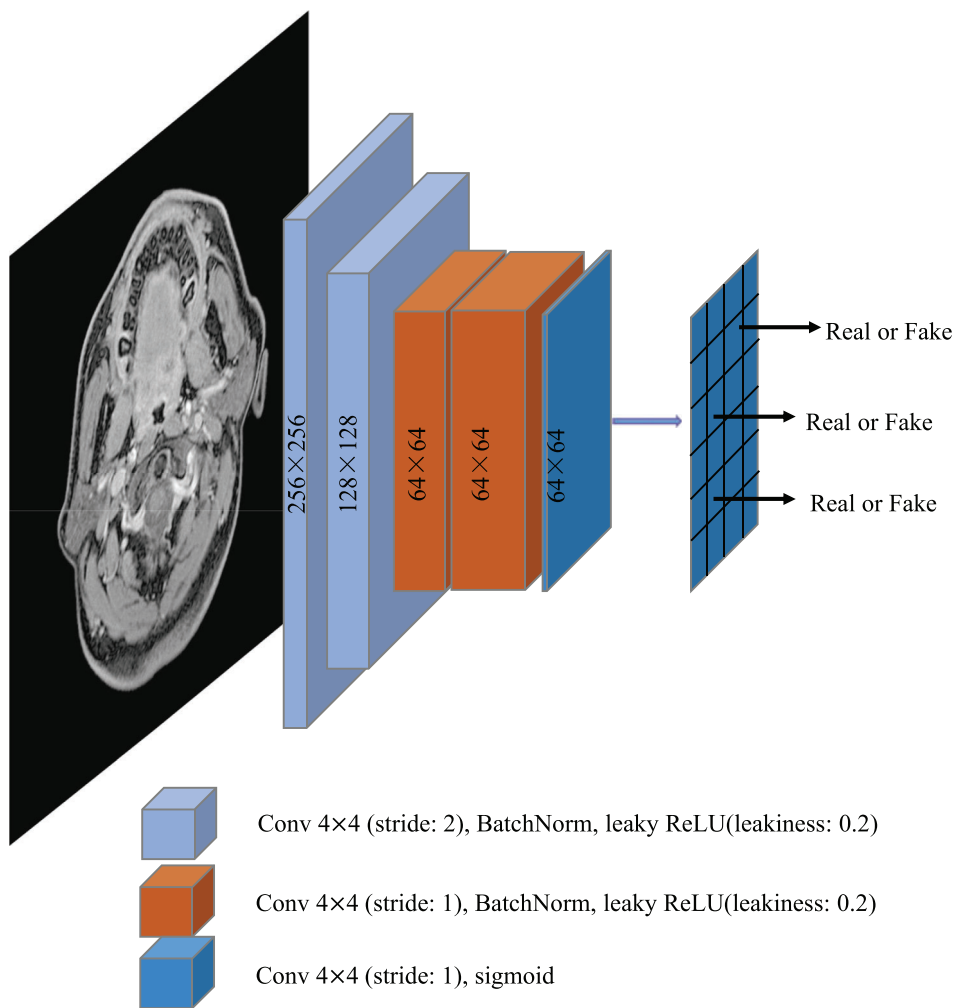


FIGURE 4 Structure diagram of the discriminator in MARINet.

learning rate of 1×10^{-4} , $\beta_1 = 0.5$, $\beta_2 = 0.9$. We empirically set $\lambda_1 = 100$, $\lambda_2 = 10$, and $\lambda_3 = 10$.

2.4 | Evaluation metrics

MAE, PSNR, SSIM, Fréchet Inception Distance (FID),³⁹ and SAMScore⁴⁰ were used to evaluate the inpainting effect quantitatively.

MAE quantifies the pixel value error between the inpainted MRI and real MRI images. Considering the small proportion of the mask in the image, the global MAE value was small and might not have fully reflected the inpainting effect of the artifact. Therefore, MAE for the mask (MAE_m) was used. Similarly, PSNR for the mask($PSNR_m$), SSIM, and SSIM for the mask ($SSIM_m$) were used.

FID provided a symmetric measure of the distance between two image distributions in the Inception-V3 latent space and was consistent with human judgment.

SAMScore was based on the recent high-performance Segment Anything Model (SAM) and could perform a generic semantic structural similarity metric for evaluating the faithfulness of image translation models.

2.5 | Comparison of synthetic CT before and after MRI inpainting

We trained a network to synthesize CT from MRI and compared the results of synthetic CT before and after MRI inpainting to further illustrate the importance of MRI inpainting. A total of 2400 CT images containing or near the teeth of 80 patients in our hospital from January 2019 to December 2021 were reviewed retrospectively. To quantitatively compare the effects of synthetic CT, we collected MRI and CT images from 10 patients. The 3D rigid registration between CT and MR was performed using the Elastix toolbox⁴¹ plugin on

TABLE 1 Quantitative comparison of different models on the test set.

	$MAE_m (10^{-2})$	$PSNR_m (\text{dB})$	$SSIM (\%)$	$SSIM_m (\%)$	FID	SAMscore (%)
PConv	19.38 ± 2.90	17.39 ± 0.99	98.38 ± 0.61	69.35 ± 4.01	8.32 ± 0.56	99.45 ± 0.21
GConv	19.04 ± 2.83	17.40 ± 1.03	98.58 ± 0.52	73.92 ± 3.82	7.64 ± 0.45	99.60 ± 0.12
SDEdit	18.76 ± 2.76	17.49 ± 1.08	98.61 ± 0.71	74.95 ± 4.27	7.35 ± 0.48	99.41 ± 0.13
MARINet	18.34 ± 2.75	17.62 ± 0.96	98.63 ± 0.46	75.03 ± 3.61	6.92 ± 0.39	99.69 ± 0.10
p^a	<0.01	<0.01	<0.01	<0.01	<0.01	<0.01
p^b	<0.01	<0.01	0.100	0.021	<0.01	0.024
p^c	<0.01	<0.01	0.153	0.035	0.032	0.016

p^a , p for PConv versus MARINet; p^b , p for GConv versus MARINet; p^c , p for SDEdit versus MARINet.

3Dslicer (<http://www.slicer.org>, version 4.11). CT images were acquired with a Siemens CT (SOMATOM Force, Germany) with a matrix size 512×512 , a spatial resolution of $0.98 \text{ mm} \times 0.98 \text{ mm}$, and a slice thickness of 5 mm. CT images were resampled to match the resolution of the MRI, and data augmentation techniques such as horizontal flip and random rotation were used for training. We used CycleGAN⁴² for CT synthesis from MRI, with a training epoch of 200 and a batch size 32. The generator was the U-net, whose structure was similar to UNet in MARINet, except that it was a one-encoder structure, and the discriminator was PatchGAN.³³ More details can be found in the original article.

3 | RESULTS

3.1 | Inpainting effect of models on test datasets

We performed quantitative and qualitative comparisons on the test set data to evaluate the inpainting effect of these models. Figure 5 illustrates the real image, the corrupted image, and the inpainted images by different models. Each model completed the inpainting task and generated realistic artifact inpainting images. Even when the mask covers the skin's surface, these models can effectively restore the skin's contour and edge. Concerning details, PConv was able to successfully inpaint the tissues surrounding the teeth. However, the number and contour of teeth were challenging to distinguish, and a ripple shape can be observed in the third row. The results from Gconv and SDEdit were similar to those of PConv, restoring the number and contour of teeth in some data, albeit with unclear boundaries between teeth. MARINet demonstrated superior visualization compared to the other models, capable of recovering information about soft tissue texture and tooth shape in the missing area with clear boundaries.

Table 1 provides the quantitative indicators between the real and inpainted images, represented as mean values with standard deviations. Here, MAE is calculated by normalizing the MRI pixel value to $[-1, 1]$. The MAE_m values for PConv, GConv, SDEdit, and MARINet were

0.1938, 0.1904, 0.1876 and 0.1834, respectively, and the $PSNR_m$ values were 17.39, 17.40, 17.49, and 17.62 dB, respectively. MARINet achieved the best quantitative results across six evaluation indexes. We conducted paired t-tests for the quantitative indicators between MARINet and other models to obtain a more objective assessment. All p values were less than 0.05 except for SSIM, indicating that MARINet achieved better results than the other models.

3.2 | Results of inpainting clinical MRI images with denture artifacts

Clinical MRI images with denture artifacts were used to test these models. Figure 6 displays the inpainting results of all methods. Given the lack of real images corresponding to artifact images, the evaluation effect is somewhat subjective. As observed, each model can also complete the inpainting task effectively and obtain realistic artifact inpainting images. The tooth profiles in rows 2, 4, and 6 in the SDEdit method were close to MARINet's results. Regarding details, the tooth contour boundaries rendered by PConv, and GConv are unclear. In contrast, MARINet can complete the tooth detail restoration task, providing clear contour boundaries and a reasonable number of teeth. Nonetheless, the results of all models are not satisfactory in the second and fifth rows. It may be due to the other side of the tooth in the second row being unclear, and artifacts on both sides in the fifth row degrade the quality of reference information. Despite these challenges, MARINet achieved relatively better-inpainted results than the other models.

3.3 | Ablation study

In the ablation study, we designed different experiments to investigate the effects of dual input paths, average images, and PC. We denoted different variants of the proposed model using the suffixes "w/o f_{refreg} ", "w/o MRI_a", and "w/o PC", which represent (a) no encoder f_{refreg} , (b) no MRI_a in the input, and (c) using vanilla convolution instead of PC, respectively. Figure 7 presents

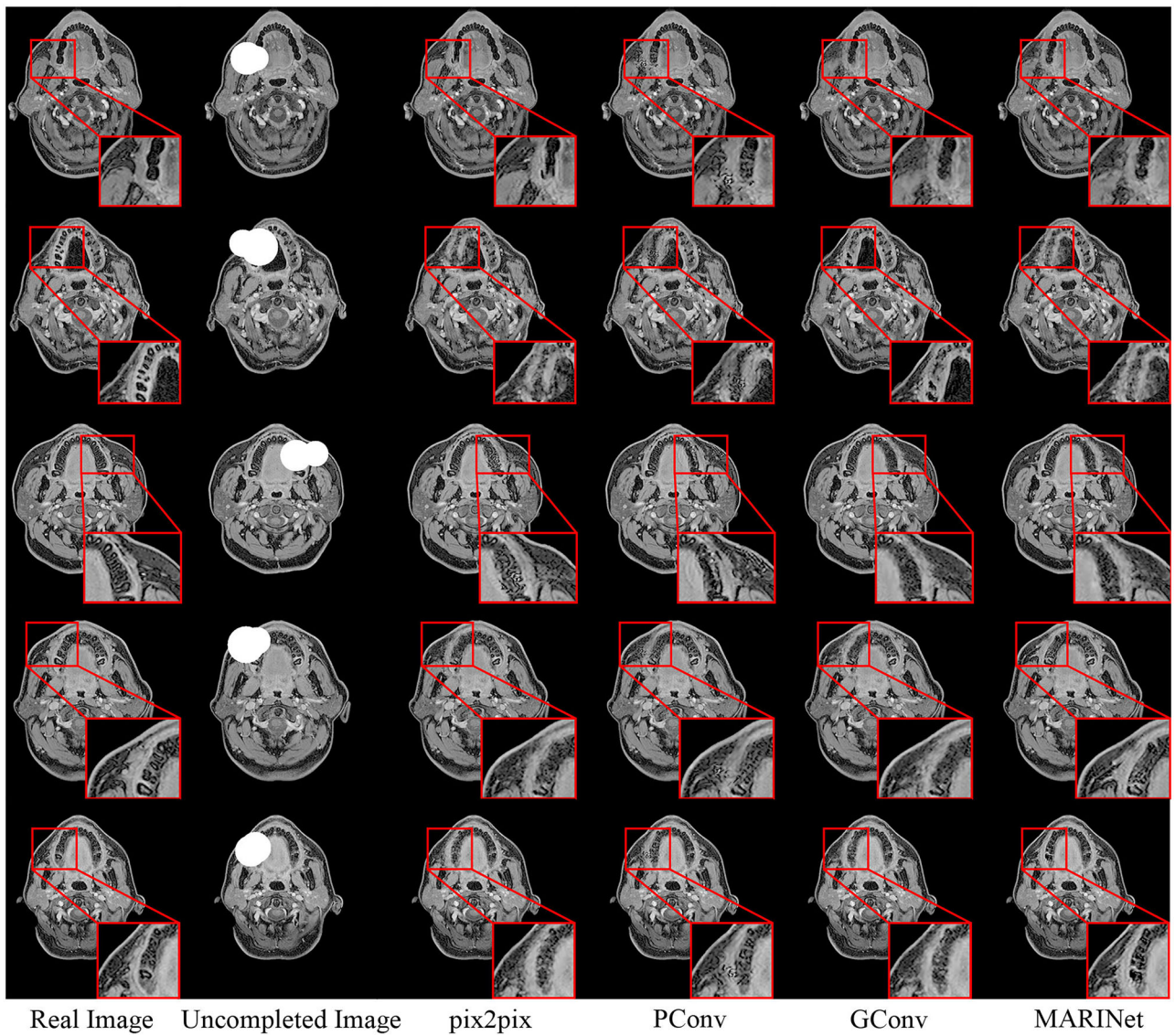


FIGURE 5 Quality comparison of the ground truth MRI images and the corrupted images, PConv, GConv, SDEdit, and MARINet results. Image pixel values were root after being normalized to [0,1]. Please zoom in to see more details.

a comparison of the results from the different variants. When f_{refreg} is omitted, the model can only obtain symmetric information from MRI_a , resulting in somewhat blurred tooth contour details. Similarly, when MRI_a is not included in the input, the model can only get symmetry information from MRI_{fr_m} in the f_{refreg} path, which also reduces the sharpness of tooth contour details. After replacing PC with ordinary convolution, f_{ori} performs the convolution calculation not from valid pixels but from all pixels and propagates this error to f_{dec} , leading to more noise perturbations in the inpainted result. Table 2 provides the quantitative results of the ablation experiments. Compared with these variants, the complete model achieved the best quantitative results. We conducted paired t-tests on the quantitative indicators between the MARINet model and MARINet variants. All p values were less than 0.05 except for SSIM and FID,

indicating that MARINet achieved better results than its variants.

3.4 | The effectiveness of mask size on the reflective registration

The mask size we utilized closely approximates the influence range of artifacts in clinical MRI, typically around 30–50 pixels (0.49 mm per pixel). To further examine the impact of mask size on reflective registration, we set up two masks, and the results of the flip registration (MRI_{fr_m}) are displayed in Figure 8. The top side comprises two adjacent 40-pixel circles, while the bottom contains two adjacent 60-pixel circles. The reflective registration yields satisfactory results for the smaller mask, and no significant deformation occurs in the tissues

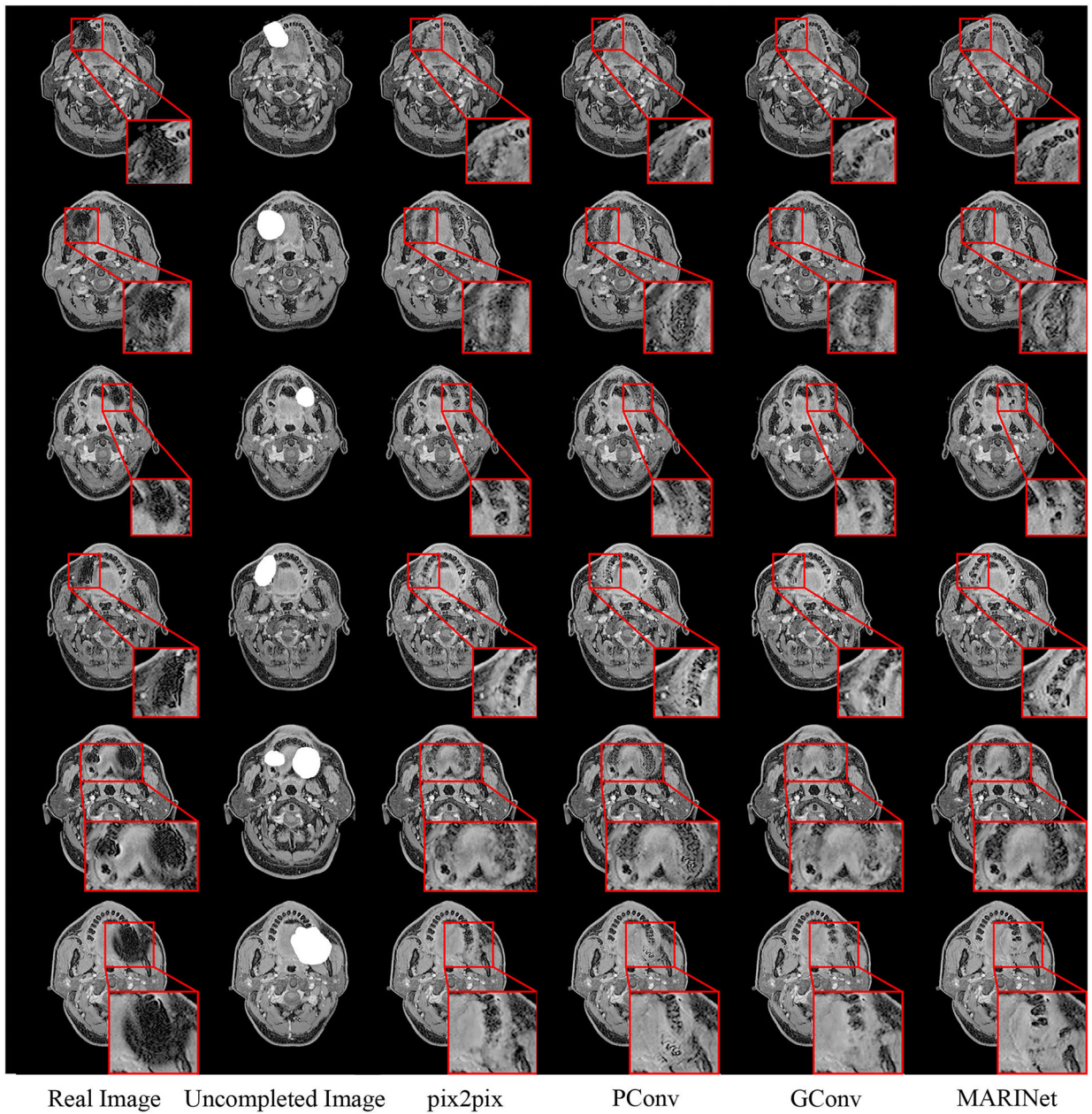


FIGURE 6 Quality comparison of the clinical MRI images and the corrupted images, PConv, GConv, SDEdit, and MARINet results. Image pixel values were root after being normalized to [0, 1]. Please zoom in to see more details.

TABLE 2 Quantitative comparison for the ablation study of MARINet.

	MAE _m (10^{-2})	PSNR _m (dB)	SSIM (%)	SSIM _m (%)	FID	SAMscore (%)
w/o f_{refreg}	19.53 ± 2.89	17.34 ± 1.06	97.38 ± 0.58	73.40 ± 3.96	7.99 ± 0.50	99.43 ± 0.12
w/o MRI _a	19.38 ± 2.91	17.39 ± 1.08	98.38 ± 0.61	73.35 ± 4.01	7.35 ± 0.46	99.52 ± 0.12
w/o PC	18.84 ± 2.83	17.51 ± 1.02	98.57 ± 0.48	74.52 ± 3.82	7.00 ± 0.45	99.51 ± 0.15
Full model	18.34 ± 2.75	17.62 ± 0.96	98.63 ± 0.46	75.03 ± 3.61	6.92 ± 0.39	99.69 ± 0.10
p ^a	<0.01	<0.01	<0.01	<0.01	<0.01	<0.01
p ^b	<0.01	<0.01	<0.01	<0.01	<0.01	0.07
p ^c	<0.01	<0.01	0.615	<0.01	0.41	0.03

^a, p for w/o f_{refreg} versus Full model; ^b, p for w/o MRI_a versus Full model; ^c, p for w/o PC versus Full model.

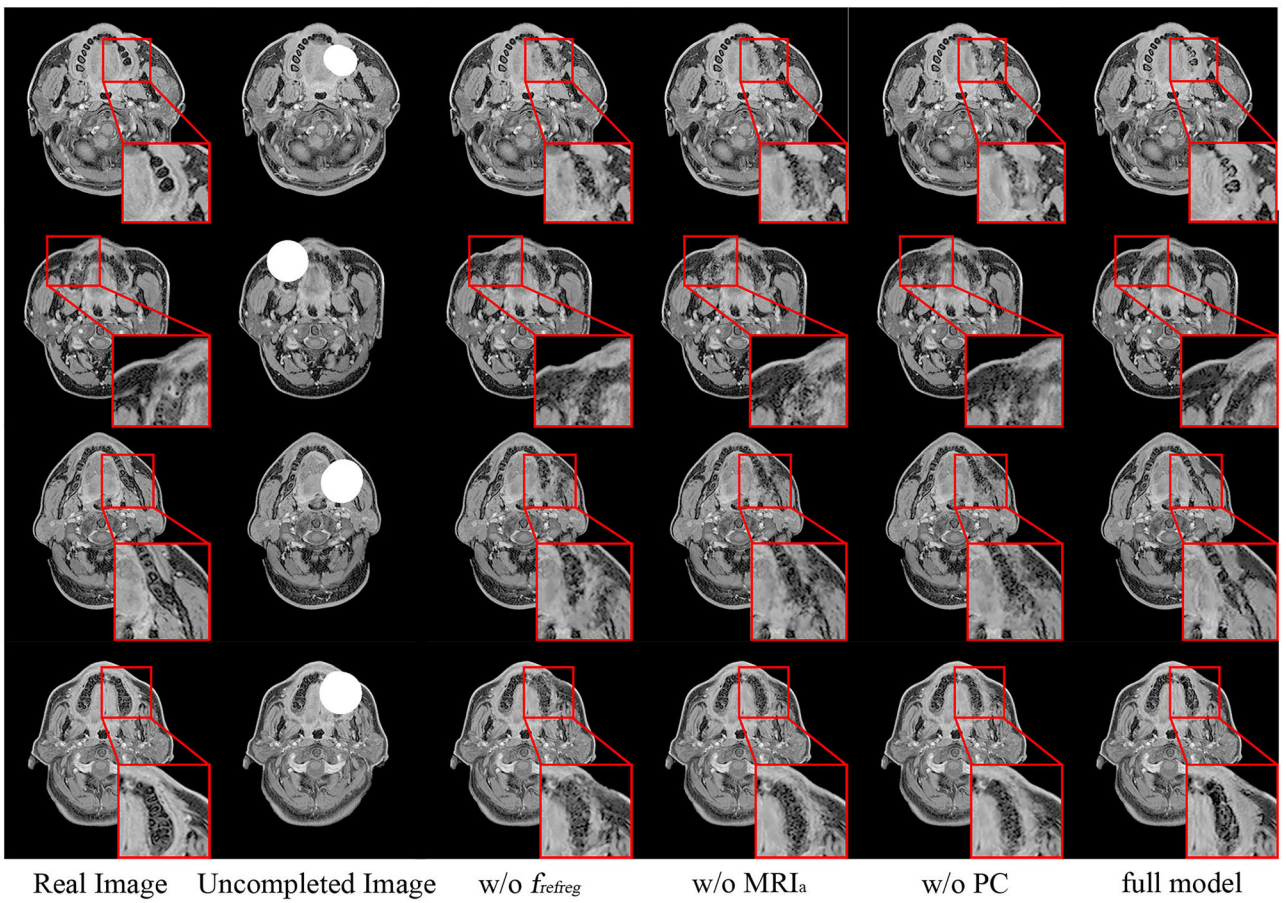


FIGURE 7 The ablation study of MARINet. Real images, uncompleted images, results without f_{refreg} , results without MRI_a , results without PC, and results of the full model are shown from top to bottom. Image pixel values were root after being normalized to [0,1]. f_{refreg} : the encoder using reflective registration image; MRI_a , the average MRI image; PC, partial convolution.

TABLE 3 Quantitative results for synthetic CT from MR.

	MAE (HU)	PSNR (dB)	SSIM (%)	FID	SAMScore(%)
cycleGAN	78.53 ± 3.87	24.34 ± 1.21	86.38 ± 1.53	18.99 ± 1.51	88.43 ± 2.12

surrounding the teeth, which is in contrast to the larger mask. Simultaneously, the inpainting results of MARINet are also presented, demonstrating a decrease in the inpainting effect when the mask surpasses a specific range.

3.5 | Comparison of synthetic CT before and after MRI inpainting

Table 3 provides the quantitative indicators between the CT and MRI images, represented as mean values with standard deviations. Synthetic CT images from normal MRI, corrupted MRI, and inpainted MRI images are shown in Figure 9. As seen from the first row, CycleGAN can initially complete the task of CT synthesis using MRI. A signal void is present in the synthetic CT image

before MRI inpainting. After inpainting, a more satisfactory CT image with tissue texture and tooth contour can be obtained.

4 | DISCUSSION

MRI images play a crucial role in clinical application. However, when a patient has a metal denture, the MRI image is distorted near the metal implant, leading to a signal void that makes soft tissue and tooth details unclear or invisible. These MRI artifacts can affect a doctor's diagnosis and image processing tasks like segmentation and registration. In clinical practice, specific scan sequences are often used to suppress metal artifacts, but these may decrease the image signal-to-noise ratio or increase the scan time.

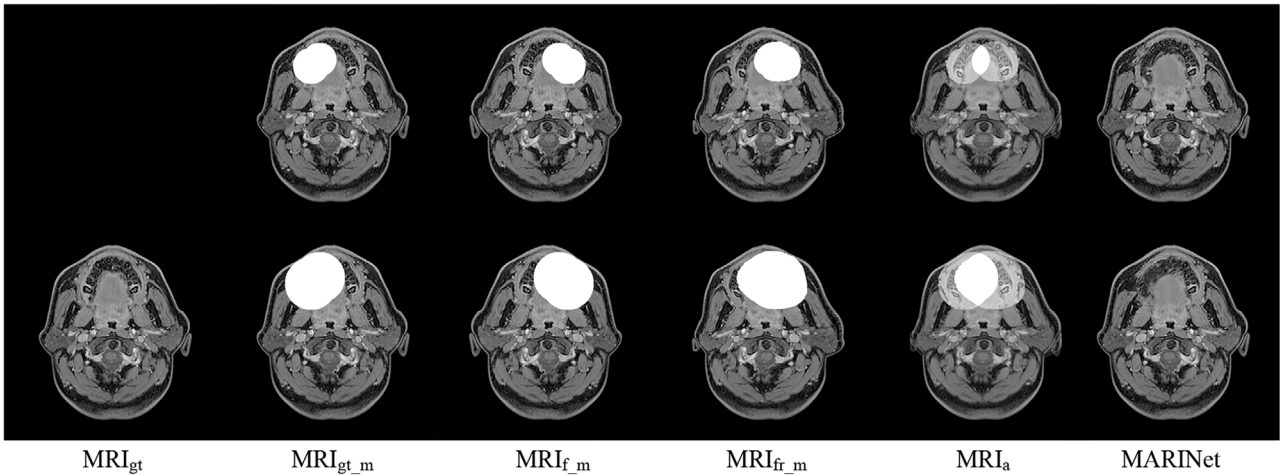


FIGURE 8 The effectiveness of mask size on the reflective registration. Left to right are the original image MRI_{gt} , corrupted image $\text{MRI}_{\text{gt_m}}$, reflective corrupted image $\text{MRI}_{\text{f_m}}$, corrupted reflective registration image $\text{MRI}_{\text{fr_m}}$, average image MRI_{a} , and MARINet result.

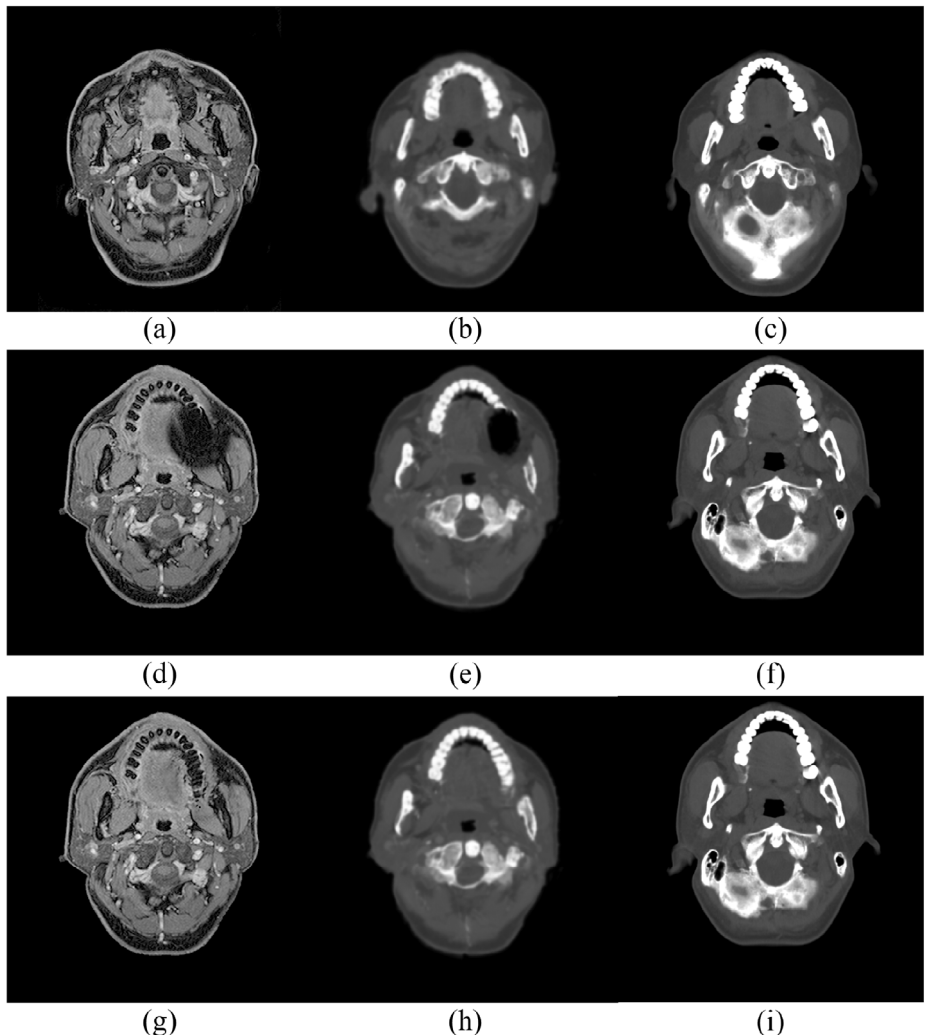


FIGURE 9 Compares synthetic CT images from normal, corrupted, and inpainted MRI images. Images (a), (b), and (c) are the test set MRI, synthetic CT, and real CT, respectively. Images (d) and (g) are the MRI containing artifacts and the inpainted MRI, respectively, while (e) and (f) are the corresponding synthetic CT images. Image (i) is the registration CT related to (d), and (f) is the CT adjacent to it. Due to different scanning dates and different head pads, MRI and CT are challenging to obtain ideal registration results.

While image inpainting methods can effectively recover data in the artifact area, these methods are not real artifact correction technologies. Nevertheless, they may be helpful for PET/MRI AC and MRI post-processing. In PET/MRI AC, an atlas registration method is usually employed. This method uses a previously acquired image template to register the collected patient images and then calculates the corresponding tissue component differences.⁴ Inpainted MRI may aid in better matching the template, thus estimating a more accurate attenuation image. Additionally, with the increasing popularity of MRI accelerators, researchers are also exploring pseudo-CT synthesis from MRI for radiotherapy planning design.⁷ More satisfactory CT images can be generated by using inpainted MRI. However, current inpainting methods can only inpaint missing data using surrounding information, and the inpainting effect is not always satisfactory. Brain MRIs exhibit inherent symmetry, so this property is extensively used in segmentation to enhance performance. Previous studies on image symmetry have predominantly used symmetric patches^{24,28} or image flip,²⁵ failing to account for the brain's natural asymmetry and rotation variance.⁴³

In response to this issue, we proposed an improved inpainting method, MARINet, which fully utilizes the quasi-symmetry of brain MRI images to achieve more realistic inpainting results. MARINet is U-Net-based and adopts a dual-path encoder to learn features from both the original and reflectively registered images. It uses these features to gradually recover the information in the artifact region during the decoding process. Inspired by the success of a dual-stream encoder-decoder architecture in multimodal segmentation,^{44,45} we utilized the original image and the flipped registration image in two separate encoders to maximize feature extraction for inpainting the missing region. U-Net was selected as the backbone because of its ability to handle global and local features in image spatial domain,²⁷ aligning with our goal of recovering global contours and local details (like tooth slots and tooth shape) in image inpainting.⁴⁴ Additionally, MARINet adopts PCs to concentrate the convolution operation on effective pixels, thereby reducing the impact of invalid pixel values on the output.

The anatomical results showed a relatively small difference in the soft tissue between the repaired MRI images by MARINet and the real MRI images. MARINet restored the number and contour of the teeth, which was difficult to achieve using previous methods. The quantitative results demonstrated the superior inpainting performance of MARINet compared to other classical networks. In a similar study, Xing et al.³ proposed a deep network-based image inpainting framework to replace tumor regions with synthetic normal tissues. In the quantitative analysis, for the test data of T1, T1-weighted contrast-enhanced, and T2, the SSIM in the inpainting results were 0.9823, 0.9595, and 0.9573, respectively.

These values are comparable to the results of our study, with 0.9863 (SSIM), indicating that image inpainting for medical images has also achieved satisfactory results.

We trained a CycleGAN network to synthesize CT from MRI to underscore the clinical significance of MRI inpainting further. The results showed that inpainted MRI synthesized more realistic CT, which may benefit PET AC in PET/MRI, CT synthesis in MRI accelerator for radiotherapy planning design, and improving image registration accuracy.

Despite its effectiveness, the application of MARINet in inpainting head MRI denture artifacts have some limitations. First, while image inpainting methods can effectively recover data in the artifact area, they are not real artifact correction technologies, and attention should be paid to their usage. Second, due to the requirement of a reflective image registration image in the input, the inpainting effect will be reduced when both left and fitting dentures are present or when the artifact region exceeds a certain threshold. Besides, the artifact areas of clinical MRI images are sketched by senior physicians, which may introduce some subjectivity. In the follow-up work, a segmentation model can be trained to better delineate the artifact region or image generation method may be tried by using MRI artifact simulation. This study serves as an initial exploration of the application of MARINet in artifact inpainting. DDPM is founded in principled probabilistic modeling and has been shown to generate diverse and high-quality images. SDEdit showed promising results with realistic contours of teeth for some examples in this work. In future studies, we plan to improve the model using DDPMs and refer to the effective pixels in normal brain MRI images to strengthen the inpainting effect. Furthermore, artifact inpainting is the first step in MRI image processing, not the final goal. Our subsequent work attempts to improve registration accuracy using inpainted MRI and apply image-synthesized CT in radiotherapy.

5 | CONCLUSION

In this study, we proposed an inpainting network (MARINet) that replaces the artifact area in MRI images with the normal brain appearance, thus reducing the impact of artifacts on image quality. Built upon U-Net, MARINet uses a dual-path encoder to learn features from both the original and reflectively registered images. Partial convolutions are employed to enhance the accuracy and reliability of the inpainting results. Our experimental results demonstrate that this method outperforms comparative methods, yielding more satisfactory results and restoring tissue texture and tooth contour, which suggest promising clinical applications for MARINet. In future work, we plan to apply this model to tasks such as MRI/CT registration and synthesis.

ACKNOWLEDGMENTS

This work is supported by the National Natural Science Foundation of China (No. 62371243), the Changzhou Sci&Tech Program (No. CJ20200099, CJ20210128, CJ20220136, and CE2023506), the Science and Technology Programs for Young Talents of Changzhou Health Commission (No. QN201932), Young Talent Development Plan of Changzhou Health Commission (No. CZQM2020075 and CZQM2020067), General Program of Jiangsu Provincial Health Commission (No. M2020006), and Jiangsu Provincial Key Research and Development Program Social Development Project (No. BE2022720), Jiangsu Provincial Medical Key Discipline Cultivation Unit of Oncology Therapeutics (Radiotherapy) (No. JSDW202237).

CONFLICT OF INTEREST STATEMENT

The authors have no conflicts to disclose.

REFERENCES

- Lee M-Y, Song K-H, Lee J-W, Choe B-Y, Suh TS. Metal artifacts with dental implants: evaluation using a dedicated CT/MR oral phantom with registration of the CT and MR images. *Sci Rep.* 2019;9(1):754.
- Hyun CM, Bayaraa T, Yun HS, Jang TJ, Park HS, Seo JK. Metal artifact reduction with intra-oral scan data for 3D low dose maxillofacial CBCT modeling. *arXiv preprint arXiv:220203571.* 2022.
- Xing F, Liu X, Kuo J, Fakhri G, Woo J. Brain MR atlas construction using symmetric deep neural inpainting. *IEEE J Biomed Health Inform.* 2022;26(7):3185-3196.
- Arabi H, Zaidi H. Three-dimensional shape completion using deep convolutional neural networks: application to truncation compensation and metal artifact reduction in PET/MRI attenuation correction. *2019 IEEE Nuclear Science Symposium and Medical Imaging Conference (NSS/MIC).* 2019:1-3.
- Han R, Jones CK, Lee J, et al. Joint synthesis and registration network for deformable MR-CBCT image registration for neurosurgical guidance. *Phys Med Biol.* 2022;67(12):125008.
- Cusumano D, Lenkowicz J, Votta C, et al. A deep learning approach to generate synthetic CT in low field MR-guided adaptive radiotherapy for abdominal and pelvic cases. *Radiother Oncol.* 2020;153:205-212.
- Sun H, Xi Q, Fan R, et al. Synthesis of pseudo-CT images from pelvic MRI images based on MD-CycleGAN model for radiotherapy. *Phys Med Biol.* 2022;67(3):035006.
- Khodarahmi I, Isaac A, Fishman EK, Dalili D, Fritz J. Metal about the hip and artifact reduction techniques: from basic concepts to advanced imaging. *Semin Musculoskelet Radiol.* 2019;23(03):e68-e81.
- Tamada D. Noise and artifact reduction for MRI using deep learning. *arXiv preprint arXiv:200212889.* 2020.
- Seo S, Do WJ, Luu HM, Kim KH, Choi SH, Park SH. Artificial neural network for Slice Encoding for Metal Artifact Correction (SEMAC) MRI. *Magn Reson Med.* 2020;84(1):263-276.
- Kwon K, Kim D, Kim B, Park H. Unsupervised learning of a deep neural network for metal artifact correction using dual-polarity readout gradients. *Magn Reson Med.* 2020;83(1):124-138.
- Kim JW, Kwon K, Kim B, Park HW. Attention guided metal artifact correction in MRI using deep neural networks. *arXiv preprint arXiv:191008705.* 2019.
- Liao H, Lin WA, Zhou SK, Luo J. ADN: artifact disentanglement network for unsupervised metal artifact reduction. *IEEE Trans Med Imaging.* 2019;39(3):634-643.
- Ranzini MB, Groothuis I, Kläser K, et al. Combining multimodal information for metal artefact reduction: an unsupervised deep learning framework. *2020 IEEE 17th International Symposium on Biomedical Imaging (ISBI).* 2020:600-604.
- Liu X, Xing F, Yang C, Kuo C-CJ, Fakhri GE, Woo J. Symmetric-constrained irregular structure inpainting for brain mri registration with tumor pathology. *International MICCAI Brainlesion Workshop.* 2020:80-91.
- Xie K, Gao L, Lu Z, et al. Inpainting the metal artifact region in MRI images by using generative adversarial networks with gated convolution. *Med Phys.* 2022;49(10):6424-6438.
- Pathak D, Krahenbuhl P, Donahue J, Darrell T, Efros AA. Context encoders: feature learning by inpainting. *Proceedings of the IEEE conference on computer vision and pattern recognition.* 2016:2536-2544.
- Iizuka S, Simo-Serra E, Ishikawa H. Globally and locally consistent image completion. *ACM Trans Graphics (ToG).* 2017;36(4):107.101-107.114.
- Liu G, Reda FA, Shih KJ, Wang T-C, Tao A, Catanzaro B. Image inpainting for irregular holes using partial convolutions. *Proceedings of the European Conference on Computer Vision (ECCV).* 2018:85-100.
- Yu J, Lin Z, Yang J, Shen X, Lu X, Huang TS. Free-form image inpainting with gated convolution. *Proceedings of the IEEE/CVF International Conference on Computer Vision (ICCV).* 2019:4471-4480.
- Armanious K, Mecky Y, Gatidis S, Yang B. Adversarial inpainting of medical image modalities. *IEEE International Conference on Acoustics, Speech and Signal Processing (ICASSP).* 2019:3267-3271.
- Armanious K, Kumar V, Abdulatif S, Hepp T, ipA-MedGAN YangB, : Inpainting of arbitrarily regions in medical modalities. *2020 IEEE International Conference on Image Processing (ICIP).* 2020:3005-3009.
- Zhang X, Wang X, Shi C, et al. DE-GAN: domain embedded gan for high quality face image inpainting. *Pattern Recogn.* 2022;124:108415.
- Wang Y, Katsaggelos AK, Wang X, Parrish TB, A deep symmetry convnet for stroke lesion segmentation. *2016 IEEE International Conference on Image Processing (ICIP).* 2016:111-115.
- Shen H, Zhang J, Zheng W, Efficient symmetry-driven fully convolutional network for multimodal brain tumor segmentation. *2017 IEEE International Conference on Image Processing (ICIP).* 2017:3864-3868.
- Chen H, Qin Z, Ding Y, Tian L, Qin Z. Brain tumor segmentation with deep convolutional symmetric neural network. *Neurocomputing.* 2020;392:305-313.
- Ronneberger O, Fischer P, Brox T, U-net: convolutional networks for biomedical image segmentation. *International Conference on Medical image computing and computer-assisted intervention.* 2015:234-241.
- Wu X, Bi L, Fulham M, Feng DD, Zhou L, Kim J. Unsupervised brain tumor segmentation using a symmetric-driven adversarial network. *Neurocomputing.* 2021;455:242-254.
- Raina K, Yahorau U, Schmah T. Exploiting bilateral symmetry in brain lesion segmentation with reflective registration. In: Soares F, Fred A, Gamboa H, eds. *Bioimaging.* SciTePress; 2020:116-122.
- Lowe kamp BC, Chen DT, Ibáñez L, Blezek D. The design of SimpleITK. *Front Neuroinform.* 2013;7:45.
- Ueda J, Okajima K. Face morphing using average face for subtle expression recognition. *2019 11th International Symposium on Image and Signal Processing and Analysis (ISPA).* 2019:187-192.
- Cao J, Hu Y, Yu B, He R, Sun Z. Load balanced gans for multi-view face image synthesis. *arXiv preprint arXiv:180207447.* 2018.
- Isola P, Zhu J, Zhou T, Efros AA. Image-to-image translation with conditional adversarial networks. *Comput Vision Pattern Recogn.* 2017:5967-5976.

34. Mao X, Li Q, Xie H, Lau RY, Wang Z, Paul Smolley S. Least squares generative adversarial networks. *Proceedings of the IEEE international conference on computer vision*. 2017:2794-2802.
35. Largent A, Barateau A, Nunes J-C, et al. Pseudo-CT generation for MRI-only radiation therapy treatment planning: comparison among patch-based, atlas-based, and bulk density methods. *Int J Radiat Oncol Biol Phys*. 2019;103(2):479-490.
36. Meng C, He Y, Song Y, et al. SDEdit: guided image synthesis and editing with stochastic differential equations. *arXiv preprint arXiv:210801073*. 2021.
37. Ho J, Jain A, Abbeel P. Denoising diffusion probabilistic models. *Adv Neural Inform Process Syst*. 2020;33:6840-6851.
38. Song Y, Sohl-Dickstein J, Kingma DP, Kumar A, Ermon S, Poole B. Score-based generative modeling through stochastic differential equations. *arXiv preprint arXiv:201113456*. 2020.
39. Heusel M, Ramsauer H, Unterthiner T, Nessler B, Hochreiter S. Gans trained by a two time-scale update rule converge to a local nash equilibrium. *Adv Neural Inform Process Syst*. 2017;30:6629-6640.
40. Li Y, Chen M, Yang W, et al. SAMScore: a semantic structural similarity metric for image translation evaluation. *arXiv preprint arXiv:230515367*. 2023.
41. Klein S, Staring M, Murphy K, Viergever MA, Pluim JP. Elastix: a toolbox for intensity-based medical image registration. *IEEE Trans Med Imaging*. 2009;29(1):196-205.
42. Zhu J-Y, Park T, Isola P, Efros AA. Unpaired image-to-image translation using cycle-consistent adversarial networks. *Proceedings of the IEEE international conference on computer vision*. 2017:2223-2232.
43. Vupputuri A, Ashwal S, Tsao B, Ghosh N. Ischemic stroke segmentation in multi-sequence MRI by symmetry determined superpixel based hierarchical clustering. *Comput Biol Med*. 2020;116:103536.
44. Valindria VV, Pawlowski N, Rajchl M, et al. Multimodal learning from unpaired images: application to multi-organ segmentation in CT and MRI. *2018 IEEE winter conference on applications of computer vision (WACV)*. 2018:547-556.
45. Zhou T, Ruan S, Canu S. A review: deep learning for medical image segmentation using multi-modality fusion. *Array*. 2019;3:100004.

How to cite this article: Xie K, Gao L, Zhang H, et al. GAN-based metal artifacts region inpainting in brain MRI imaging with reflective registration. *Med Phys*. 2023;1-15.

<https://doi.org/10.1002/mp.16724>